

Polarization ratio characteristics of electromagnetic scattering from sea ice in polar areas

Li Zhao(赵立), Tao Xie(谢涛), Lei Meng(孟雷), William Perrie, Jin-Song Yang(杨劲松), He Fang(方贺), Han Chen(陈韩), Run-Bing Ai(艾润冰)

Citation: Chin. Phys. B . 2018, 27(12): 124102. **doi:** 10.1088/1674-1056/27/12/124102
Journal homepage: http://cpb.iphy.ac.cn; http://iopscience.iop.org/cpb

What follows is a list of articles you may be interested in

Polarization ratio characteristics of electromagnetic scattering from sea ice in polar areas

Li Zhao(赵立), Tao Xie(谢涛), Lei Meng(孟雷), William Perrie, Jin-Song Yang(杨劲松), He Fang(方贺), Han Chen(陈韩), Run-Bing Ai(艾润冰)
Chin. Phys. B . 2018, 27(12): 124102. **doi:** 10.1088/1674-1056/27/12/124102

Ultra-wideband low radar cross-section metasurface and its application on waveguide slot antenna array

Li-Li Cong(丛丽丽), Xiang-Yu Cao(曹祥玉), Tao Song(宋涛), Jun Gao(高军)
Chin. Phys. B . 2018, 27(11): 114101. **doi:** 10.1088/1674-1056/27/11/114101

Design of multi-band metasurface antenna array with low RCS performance

Si-Ming Wang(王思铭), Jun Gao(高军), Xiang-Yu Cao(曹祥玉), Yue-Jun Zheng(郑月军), Tong Li(李桐), Jun-Xiang Lan(兰俊祥), Liao-Ri Ji-Di(吉地辽日)
Chin. Phys. B . 2018, 27(10): 104102. **doi:** 10.1088/1674-1056/27/10/104102

Ultra-compact graphene plasmonic filter integrated in a waveguide

Baoxin Liao(廖宝鑫), Xiangdong Guo(郭相东), Hai Hu(胡海), Ning Liu(刘宁), Ke Chen(陈科), Xiaoxia Yang(杨晓霞), Qing Dai(戴庆)
Chin. Phys. B . 2018, 27(9): 094101. **doi:** 10.1088/1674-1056/27/9/094101

Backscattering from small-scale breaking wave turbulence structure generated by FLUENT

Luo Gen, Zhang Min
Chin. Phys. B . 2014, 23(12): 124101. **doi:** 10.1088/1674-1056/23/12/124101

Polarization ratio characteristics of electromagnetic scattering from sea ice in polar areas*

Li Zhao(赵立)[1], Tao Xie(谢涛)[2,3,†], Lei Meng(孟雷)[4], William Perrie[5], Jin-Song Yang(杨劲松)[6], He Fang(方贺)[1], Han Chen(陈韩)[1], and Run-Bing Ai(艾润冰)[1]

[1] School of Marine Sciences, Nanjing University of Information Science and Technology, Nanjing 210044, China
[2] Laboratory for Regional Oceanography and Numerical Modeling, Qingdao National Laboratory for Marine Science and Technology, Qingdao 266000, China
[3] School of Remote Sensing and Geomatics Engineering, Nanjing University of Information Science and Technology, Nanjing 210044, China
[4] Beijing City 5111 Mailbox, Beijing 100094, China
[5] Fisheries & Oceans Canada, Bedford Institute of Oceanography, Dartmouth, Nova Scotia, B2Y 4A2, Canada
[6] State Key Laboratory of Satellite Ocean Environment Dynamics, Second Institute of Oceanography, State Oceanic Administration, Hangzhou 310012, China

(Received 31 July 2018; revised manuscript received 18 September 2018; published online 10 November 2018)

In the global climate system, the polar regions are sensitive indicators of climate change, in which sea ice plays an important role. Satellite remote sensing is a significant tool for monitoring sea ice. The use of synthetic aperture radar (SAR) images to distinguish sea ice from sea water is one of the current research hotspots in this topic. To distinguish sea ice from the open sea, the polarization ratio characteristics of sea ice and sea water are studied for L-band and C-band radars, based on an electromagnetic scattering model of sea ice derived from the integral equation method (IEM) and the radiative transfer (RT) model. Numerical experiments are carried out based on the model and the results are given as follows. For L-band, the polarization ratio for sea water depends only on the incident angle, while the polarization ratio for sea ice is related to the incident angle and the ice thickness. For C-band, the sea water polarization ratio is influenced by the incident angle and the root mean square (RMS) height of the sea surface. For C-band, for small to medium incident angles, the polarization ratio for bare sea ice is mainly determined by the incident angle and ice thickness. When the incident angle increases, the RMS height will also affect the polarization ratio for bare sea ice. If snow covers the sea ice, then the polarization ratio for sea ice decreases and is affected by the RMS height of snow surface, snow thickness, volume fraction and the radius of scatterers. The results show that the sea ice and the open sea can be distinguished by using either L-band or C-band radar according to their polarization ratio difference. However, the ability of L-band to make this differentiation is higher than that of C-band.

Keywords: sea ice, electromagnetic scattering, polarization ratio

PACS: 41.20.Jb, 84.40.Xb, 91.50.Iv, 92.10.Rw **DOI:** 10.1088/1674-1056/27/12/124102

1. Introduction

Sea ice covers about 7% of the earth's surface and 12% of the world's oceans. Much of the world's sea ice is enclosed within the polar ice packs. Although sea ice is mainly distributed in the cold regions far from human settlements, sea ice has attracted close attention because it is an important part of the climate system. Changes in sea ice have significant influences on weather and climate through complex feedback processes, and thus have become an important indicator of global climate change. Therefore, the use of space-based radar to detect sea ice and change in sea ice in polar region is of great scientific significance and application value.

Synthetic aperture radar (SAR) is an active earth observation system that can work day and night in almost all-weather, without limitation due to clouds, but has limited capability to penetrate the surface beneath. Since its initial launch on Seasat in 1978, SAR has been used for earth observation, especially ocean observations, including sea surface wind field retrieval,[1] oil spill monitoring,[2,3] target identification,[4] sea ice monitoring,[5] ocean current inversion,[6–8] and other fields. Among them, the sea ice monitoring by remote sensing has attracted increasing attention, and focuses mainly on the identification and classification of sea ice. At present, image texture analysis,[9–12] neural network methods,[13,14] support vector machine methodologies[15,16] are mainly used. These methods usually rely on the remote sensing imagery itself; few of them identify and classify sea ice based on the electromagnetic scattering mechanism.

In this work, our study is based on the electromagnetic scattering model for remote sensing parameter retrieval and the scattering characteristics of sea ice. The traditional random rough surface scattering models mainly include the small disturbance model (SPM) and the Kirchhoff model (KA).[17–20] The SPM is suitable for slightly rough surfaces, while the KA

*Project supported by the National Key Research and Development Program of China (Grant No. 2016YFC1401007), the Global Change Research Program of China (Grant No. 2015CB953901), the National Natural Science Foundation of China (Grant No. 41776181), and the Postgraduate Research & Practice Innovation Program of Jiangsu Province, China (Grant No. KYCX18_1012).

†Corresponding author. E-mail: xietao@nuist.edu.cn

© 2018 Chinese Physical Society and IOP Publishing Ltd

is mainly used for rough surfaces with large surface curvature. Based on these models, a series of models has been developed, including small slope approximation (SSA)[21–24] and integral equation model (IEM).[25–27] For slightly rough surfaces, the IEM can be simplified into SPM; under the Kirchhoff approximation, the IEM is equivalent to the KA. Compared with other scattering models, IEM has high precision and wide application range, and has received much attention.

According to the IEM and radiative transfer (RT) model, some researchers have studied the electromagnetic scattering properties of sea ice. Wakabayashi *et al.*[28] studied the polarimetric characteristics of sea ice in the Sea of Okhotsk observed by airborne L-band SAR. They found that the backscattering coefficients, and particularly the vertical (VV) to horizontal (HH) backscattering ratio, are highly correlated with ice thickness. A simple simulation using IEM was conducted to study the relations among these variables, by using the physical parameters of typical sea ice. Liu *et al.*[29] developed a sea-ice microwave scattering mechanism for thin sea ice with slight roughness in the Bohai Sea as observed in the winter of 2012 according to the backscattering coefficients, which were measured under the condition of the three bands (L, C, and X), two polarizations (HH and VV), and incident angles of 20°–60°, by using a ground-based scatterometer. Theoretical results were obtained based on IEM and RT models and compared with the measurements. Nakamura *et al.*[30] carried out sea ice thickness retrieval in the Sea of Okhotsk by using dual-polarization SAR data. They developed an algorithm for retrieving the ice thickness, which is based on the backscattering ratio and IEM. In Syahali and Ewe's work,[31] multiple-surface scattering, based on IEM that calculates surface scattering and additional second-order surface-volume scattering, was added into the model (based on prior studies) for improvement in the backscattering calculation.

The SAR-based sea ice classification and identification are very important in the research of ocean and polar remote sensing. Traditional classification methods concentrate on the SAR images themselves, ignoring the physical mechanism. In our work, we will investigate the polarization ratio characteristics of sea water and sea ice (with or without snow-cover) based on the electromagnetic scattering mechanism. The results will demonstrate that the difference between the polarization ratios of sea water and sea ice can be used to discriminate sea ice from sea water.

In the second section of this paper, an electromagnetic scattering model for a random rough surface is derived from IEM and RT theory, based on a geometric electromagnetic scattering model for a layered medium. In the third section, based on the above model, the polarization ratios for sea ice and water under different conditions are numerically simulated. The polarization ratio characteristics of sea water and sea ice (bare and snow-covered) for C-band and L-band are studied. The last section draws the conclusions from the present study.

2. Electromagnetic scattering model of sea ice

2.1. Sea ice physical model

The physical model for sea ice includes both internal structure (such as salinity, brine and bubbles, including their size, distribution, and concentration) and external characteristics (such as surface roughness, thickness, and related characteristics) that influence the microwave scattering characteristics of sea ice as illustrated in Fig. 1. The incident angle and transmitted angle of the electromagnetic wave are θ and θ_t, respectively. The transmitted wave is scattered by the scatterers embedded in the sea ice at the air–ice interface, and the corresponding incident and scattering angle are represented as θ_0 and θ_s, respectively. The thickness of the sea ice is d.

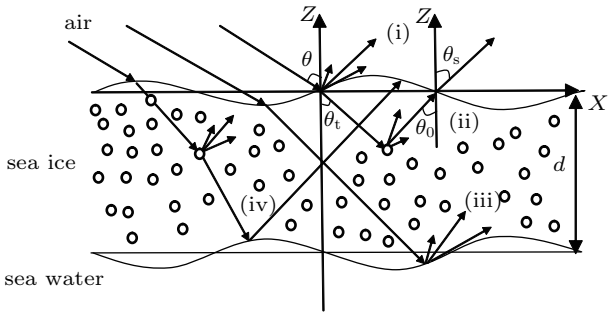


Fig. 1. Physical and microwave scattering model of sea ice, showing (i) top surface scattering, (ii) volume scattering, (iii) bottom surface scattering, and (iv) scattering due to surface–volume interactions.

2.2. Sea ice electromagnetic scattering model

The sea ice electromagnetic scattering includes several components: (i) top surface scattering from the air–ice interface, (ii) volume scattering from the scatterers in the sea ice, (iii) bottom surface scattering from the ice–water interface, and (iv) scattering from the interaction of the surfaces and the scatterers as shown in Fig. 1 clearly. Therefore, according to these four components, the total bistatic scattering coefficients of sea ice can be described as follows:[29]

$$\sigma^0 = \sigma_{\rm ts} + \sigma_{\rm vol} + \sigma_{\rm bs} + \sigma_{\rm in}, \tag{1}$$

where σ^0 represents the total bistatic scattering coefficient, $\sigma_{\rm ts}$ the top surface scattering, $\sigma_{\rm vol}$ the volume scattering, and $\sigma_{\rm in}$ the interaction term.

Here, $\sigma_{\rm ts}$ is derived from IEM and has the following form:[27]

$$\sigma^{\rm s}_{\rm pp} = S(\theta,\theta_{\rm s})\frac{k^2}{2}\exp[-\sigma^2\left(k_z^2+k_{\rm sz}^2\right)] \times \sum_{n=1}^{\infty}\sigma^{2n}\left|I^n_{\rm pp}\right|^2\frac{W^n(k_{\rm sx}-k_x,k_{\rm sy}-k_y)}{n!}, \tag{2}$$

where k is the wave number, $k_x = k\sin\theta\cos\phi$, $k_y = k\sin\theta\sin\phi$, $k_z = k\cos\theta$, $k_{\rm sx}$, $k_{\rm sy}$ and $k_{\rm sz}$ have similar definitions by replacing θ and ϕ with $\theta_{\rm s}$ and $\phi_{\rm s}$, pp represents VV

or HH polarization, $S(\theta,\theta_s)$ is the shadowing function defined by Sancer[31] (Appendix A), σ is the RMS height of the surface, W^n is the Fourier transform of the n-th power of the surface correlation coefficient (Appendix B), and the expression for I^n_{pp} is given in Appendix C.

Top surface scattering can be expressed as

$$\sigma_{tspp} = \sigma^s_{pp}, \tag{3}$$

and bottom surface scattering has the following form:[27]

$$\sigma_{bspp} = \mu_s T(\theta_s,\theta 0)\exp(-\frac{\kappa_e d}{\mu_0})\sigma^s_{pp}(\theta_0,\theta_t;\phi_s-\phi) \times \exp\left(-\frac{\kappa_e d}{\mu_t}\right)\frac{T(\theta_t,\theta)}{\mu_t}. \tag{4}$$

The volume scattering term is derived from the RT model:[27]

$$\sigma_{volpp} = \mu_s T(\theta_s,\theta 0)a\left\{1-\exp\left[-\frac{\tau(\mu_0+\mu_t)}{\mu_0\mu_t}\right]\right\} \times \frac{P_{pp}(\mu_0,-\mu_t;\phi_s-\phi)}{\mu_0+\mu_t}\mu_t T(\theta_t,\theta), \tag{5}$$

where $\mu=\cos\theta$, $\mu_s=\cos\theta_s$, $\mu_0=\cos\theta_0$, $\mu_t=\cos\theta_t$, κ_s and κ_a are volume scattering and absorption coefficients, respectively. In terms of the above parameters, the extinction coefficient, κ_e, the albedo, a, and the optical depth, τ are found as follows: $\kappa_e=\kappa_a+\kappa_s$, $a=\kappa_s/\kappa_e$, and $\tau=\kappa_e d$, respectively. Detailed calculations of the Rayleigh parameters are given in Appendix D. Here, T is the refraction coefficient and P_{pp} represents the Rayleigh phase term,[27]

$$P_{vv} = 0.75\{2(1-\mu_t^2)(1-\mu_0^2)+\mu_t^2\mu_0^2[1+\cos 2(\phi_s-\phi)] +4\mu_0\mu_t\sqrt{(1-\mu_t^2)(1-\mu_0^2)}\cos(\phi_s-\phi)\}, \tag{6}$$

$$P_{hh} = 0.75[1+\cos 2(\phi_s-\phi)]. \tag{7}$$

The interaction term is also derived from the RT model,[27]

$$\sigma_{in} = \mu_s T(\theta_s,\theta 0)a\frac{e^{-\kappa_e d/\mu_0}-e^{-\kappa_e d/\mu_t}}{\mu_0-\mu_t} \times T(\theta_t,\theta)\,e^{-k_l^2\sigma_b^2(\mu_0+\mu_t)^2} \times\left[\mu_0 R(\theta_0)P(-\mu_0,-\mu_t;\phi_s-\phi)\,e^{-\kappa_e d/\mu_0} +\mu_t R(\theta_t)P(\mu_0,\mu_t;\phi_s-\phi)\,e^{-\kappa_e d/\mu_t}\right]. \tag{8}$$

For the backscattering case, $\theta=\theta_s$, $\phi=0$, and $\phi_s=\pi$. Thus, the backscattering coefficients of sea ice can be calculated from Eq. (1) to Eq. (8).

The polarization ratio of sea ice is defined as follows:

$$PR_i = \sigma^0_{VV}/\sigma^0_{HH}. \tag{9}$$

The normalized form of the PR_i is

$$PR = 10\log 10(PR)\,dB. \tag{10}$$

From Eq. (1) to Eq. (10), the backscattering coefficients and corresponding polarization ratio of sea ice can be calculated. Next, numerical experiments are carried out to study the polarization ratio characteristics of seawater, bare and snow-covered sea ice, for both L-band backscatter and C-band backscatter.

3. Numerical results

3.1. Polarization ratio characteristics of seawater

The ability of microwave radar to penetrate sea water is weak, and the penetration depths at C-band and L-band are about 0.4 cm and 3 cm, respectively.[29] Therefore, microwave electromagnetic scattering mainly acts on the sea surface, generating surface scattering, which can be calculated by the integral equation method (IEM). The electromagnetic scattering of seawater is mainly related to incident angle, electromagnetic wave frequency and wind speed. The wind speed affects the sea surface roughness (characterized by the RMS height and the correlation length), which in turn affects the radar backscattering cross-section.

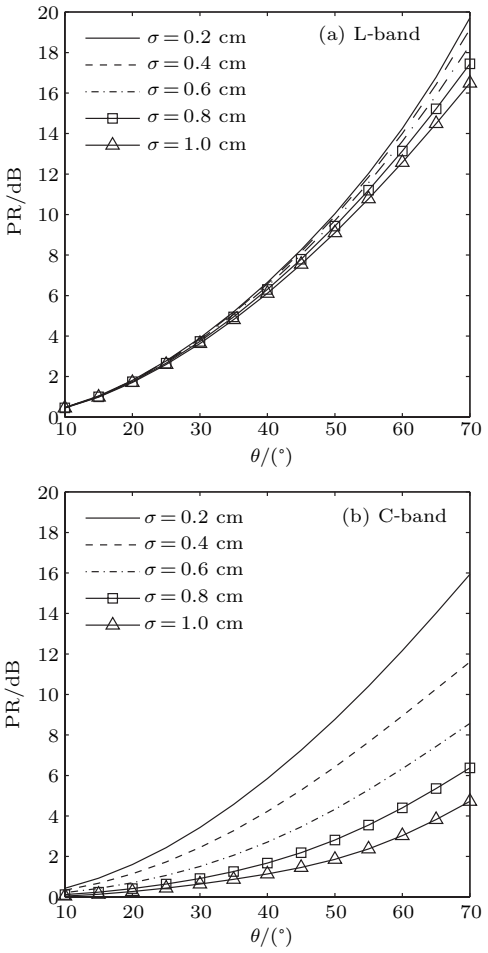


Fig. 2. Variations of polarization ratio of seawater with RMS height of sea surface for (a) L-band and (b) C-band. The correlation length is 5 cm, the dielectric constant of seawater for L-band and C-band are $82.70+j23.88$ and $64.21+j37.52$, respectively.

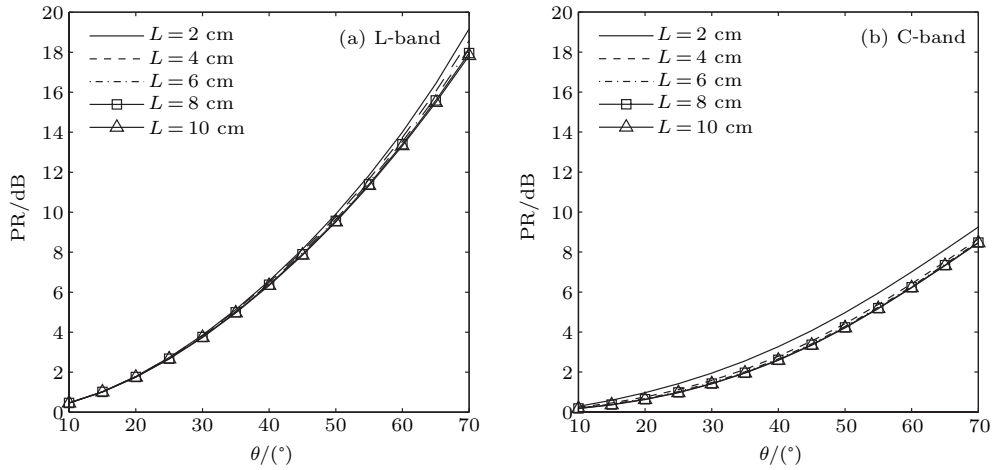


Fig. 3. Variations of polarization ratio of seawater with correlation length of sea surface for: (a) L-band and (b) C-band. RMS height is 0.6 cm, dielectric constant of seawater for L-band and C-band are $82.70 + \mathrm{j}23.88$ and $64.21 + \mathrm{j}37.52$, respectively.

For L-band and C-band radars, the variations of the polarization ratio of seawater with the RMS height of the sea surface are shown in Figs. 2(a) and 2(b), respectively. The C-band and L-band polarization ratio of seawater increase with incident angle and decrease with RMS height of the sea surface. By comparison, the polarization ratio is more sensitive to RMS height for C-band than that for L-band. At small-to-medium incident angles, the L-band seawater polarization ratio hardly varies with the RMS height. As shown in Fig. 3, the seawater polarization ratio remains almost constant as the correlation length of the sea surface increases, at both C and L band. In addition, we also find that the L-band seawater polarization ratio is greater than the C-band sea ice polarization ratio.

3.2. Polarization ratio characteristics of bare sea ice

In this subsection, the polarization ratios of bare sea ice under different physical conditions are simulated. Simulation parameters used in the model are given in Table 1.

Table 1. Simulation parameters for bare sea ice.

Variable	Parameter	Simulation value
f	frequency	1.25 GHz for L-band, 5.3 GHz for C-band
σ_1	RMS height of air–ice interface	0.4 cm
σ_2	RMS height of ice–water interface	0.2 cm
L_1	correlation length of air–ice interface	5 cm
L_2	correlation length of ice–water interface	3 cm
ε_{r}	dielectric constant of scatterers in the sea ice	$82.70 + \mathrm{j}23.88$ for L-band, $64.21 + \mathrm{j}37.52$ for C-band
$\varepsilon_{\mathrm{ri}}$	dielectric constant of sea ice	$3.4 + \mathrm{j}0.22$
$\varepsilon_{\mathrm{rw}}$	dielectric constant of seawater	$82.70 + \mathrm{j}23.88$ for L-band, $64.21 + \mathrm{j}37.52$ for C-band
d	sea ice thickness	20 cm
fv	volume fraction of scatterers	10%
r	scatterer radius	0.25 mm

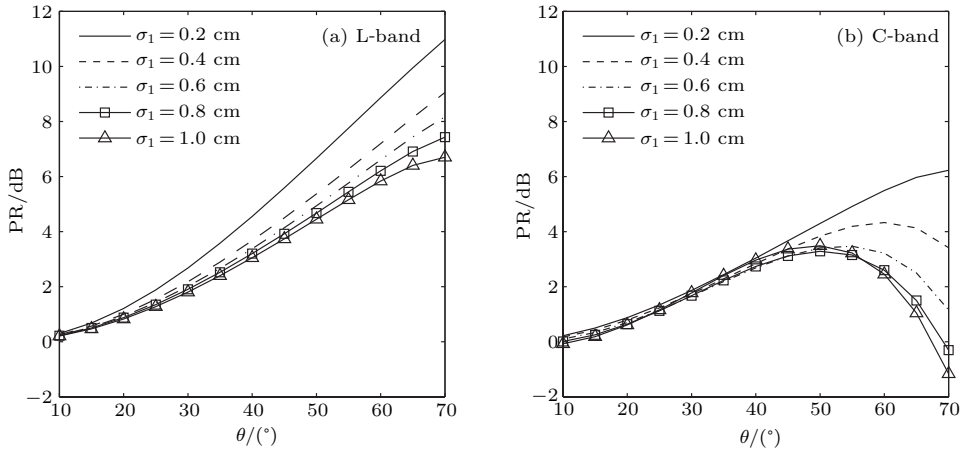


Fig. 4. Variations in bare sea ice polarization ratio with RMS height of ice surface for: (a) L-band and (b) C-band.

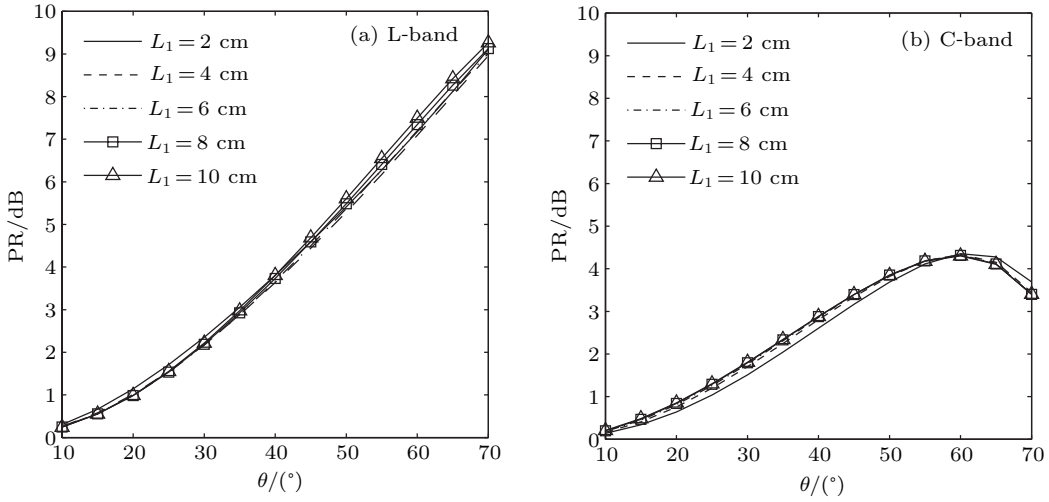


Fig. 5. Variations in bare sea ice polarization ratio with correlation length of ice surface for: (a) L-band and (b) C-band.

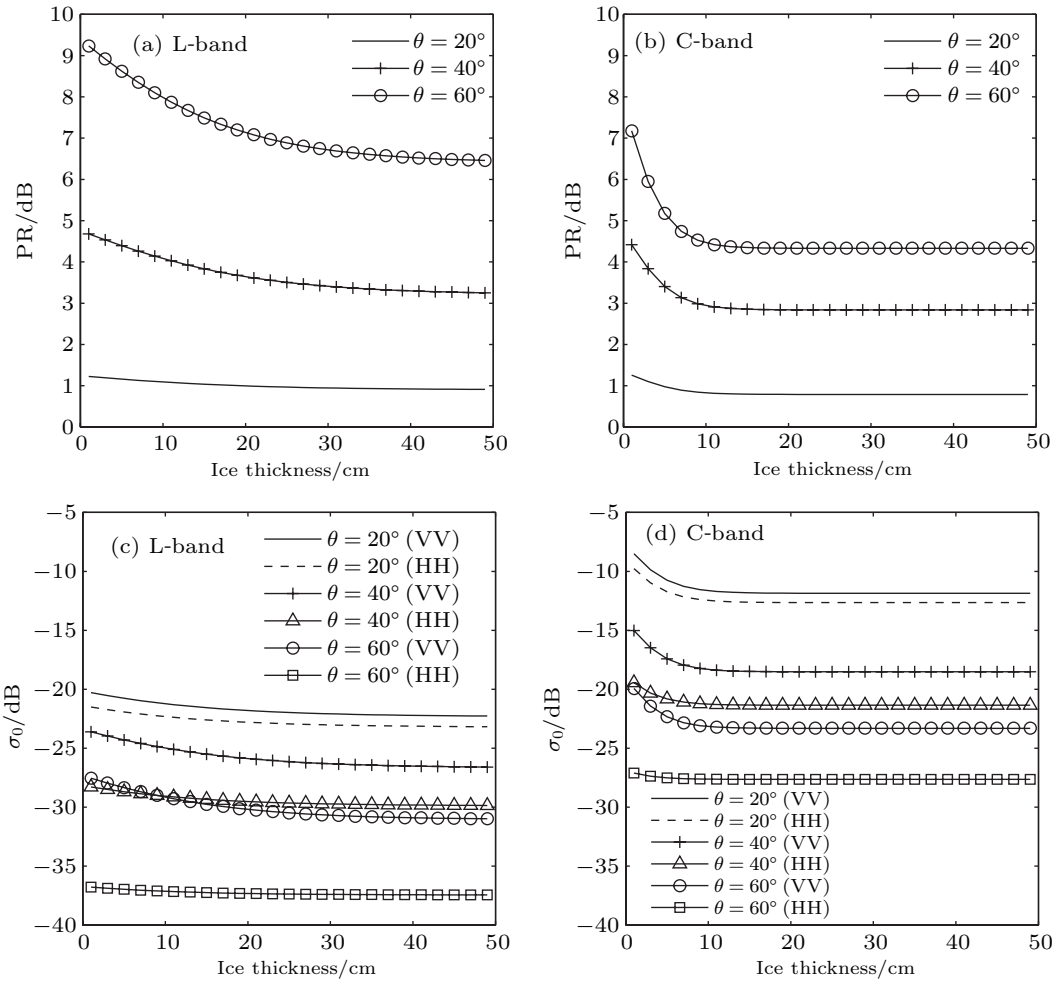


Fig. 6. Variations in bare sea ice polarization ratio with ice thickness at three typical incident angles for (a) L-band and (b) C-band, and corresponding variations of backscattering coefficients for (c) L-band and (d) C-band.

As shown in Fig. 4(a), the L-band bare sea ice polarization ratio increases with incident angle increasing and decreases with RMS height of the ice surface increasing. When incident angles are smaller than about 45°, the C-band bare sea ice polarization ratio hardly changes with RMS height increasing; when incident angles are greater than 45°, the polarization ratio decreases with the RMS height increasing (Fig. 4(b)). For both C and L-bands, the bare sea ice polarization ratio hardly changes with correlation length (Fig. 5).

The variations in bare sea ice polarization ratio with ice thickness at three typical incident angles are shown in Figs. 6(a) and 6(b). The former decreases as ice thickness increases and remains constant after the ice thickness has reached a critical value, which is mainly related to the penetra-

tion depth of electromagnetic wave. Because the penetration depth of L-band for sea ice is greater than that of C-band, the L-band sea ice polarization ratio is more sensitive to change in sea ice thickness than the C-band sea ice polarization ratio. At small incident angles, electromagnetic scattering is dominated by surface scattering, and the polarization ratio hardly changes with ice thickness. As the incident angle increases, the sea ice polarization ratio also increases; that is, the difference between VV polarization and HH polarization increases, which is mainly caused by bottom surface scattering and volume scattering. The corresponding variations in backscattering coefficient with ice thickness are shown in Figs. 6(c) and 6(d), which have similar trends to the variation of the polarization ratio with ice thickness. The backscattering coefficients of bare ice decrease with the incident angle for both L- and C-bands, due to the dominant specular scattering mechanism, over the large angular domain.

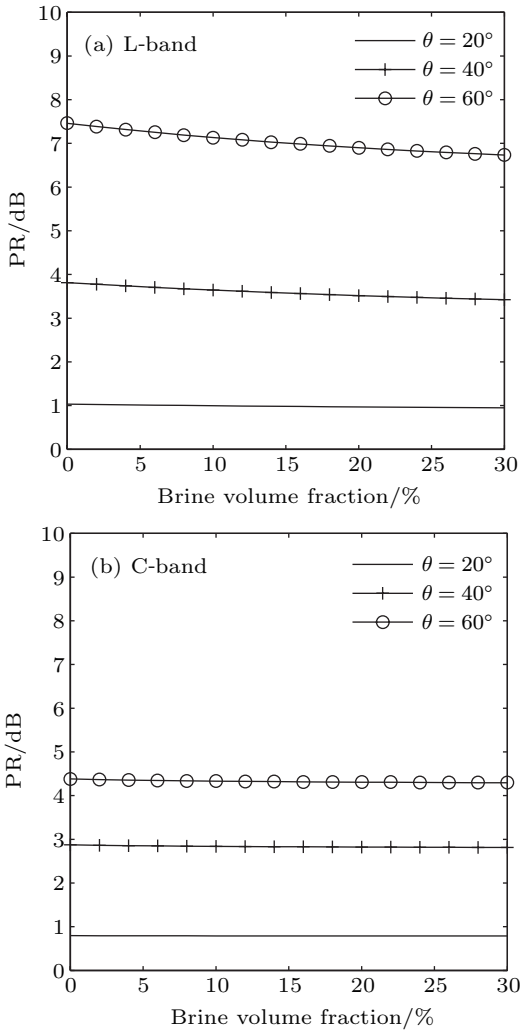


Fig. 7. Variations of the bare sea ice polarization ratio with brine volume fraction at three typical incident angles for: (a) L-band and (b) C-band.

The scatterers in the sea ice (mainly brines and bubbles) are the source of the volume scattering and bottom-volume scattering interaction. Since the interaction is weak, only 'single-bounce' interaction is considered. In the experiment, we only consider brines. Figures 7 and 8 show the polarization ratios as a function of the volume fraction and radius of scatterer, for different incident angles and radar bands. In both bands, the polarization ratio decreases slightly with volume fraction and radius of the scatterer. The influences of these two parameters on the bare sea ice polarization ratio are negligible. This indicates that the volume scattering has little effect on bare sea ice polarization ratio for both L-band and C-band.

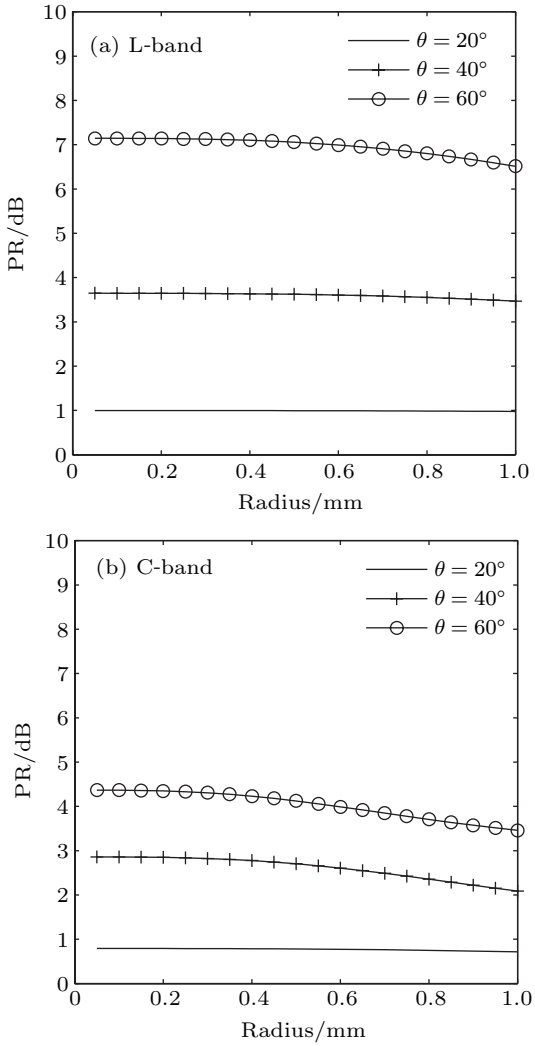


Fig. 8. Variations of the bare sea ice polarization ratio with scatterer radius at three typical incident angles for (a) L-band and (b) C-band.

3.3. Polarization ratio characteristics of snow-covered sea ice

Snow may have a significant influence on the polarization ratio characteristics of sea ice. Similarly, the total backscattering now consists of the top surface scattering from the air-snow interface, volume scattering in the snow, bottom surface scattering from the snow-ice interface and bottom-volume scattering interaction. To study the effect of snow on the sea ice polarization ratio, numerical experiments were carried out based on the above scattering model. The parameters set in the model are shown in Table 2.

Table 2. Simulation parameters for snow-covered sea ice.

Variable	Parameter	Simulation value
f	frequency	1.25 GHz for L-band, 5.3 GHz for C-band
σ_1	RMS height of air-snow interface	0.4 cm
σ_2	RMS height of snow-ice interface	0.2 cm
L_1	correlation length of air-snow interface	5 cm
L_2	correlation length of snow-ice interface	3 cm
ε_r	dielectric constant of scatterers in the snow	$4.13+j0.38$
ε_{ri}	dielectric constant of sea ice	$4.13+j0.38$
ε_{rs}	dielectric constant of snow	$1.6+j0.55$
d	snow thickness	20 cm
fv	volume fraction of scatterers	20%
r	scatterer radius	0.5 mm

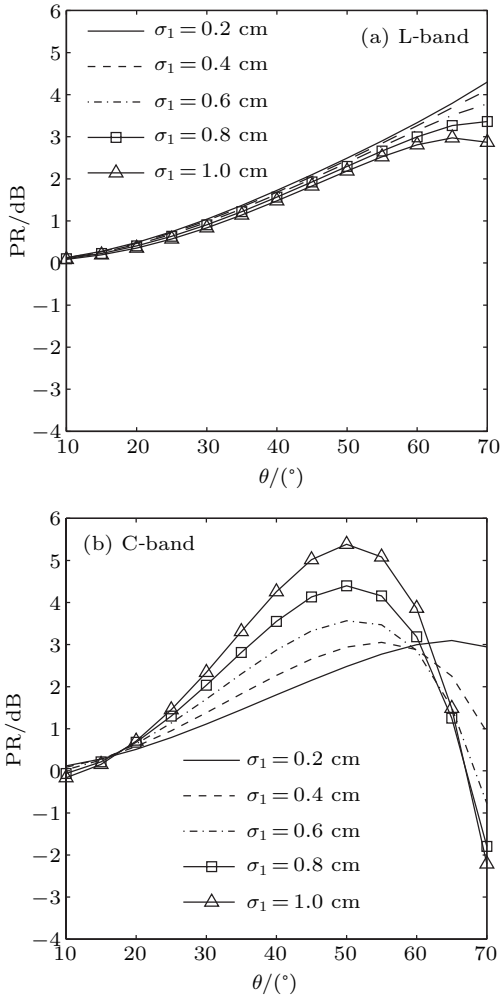


Fig. 9. Variations of snow-covered sea ice polarization ratio with RMS height of snow surface for (a) L-band and (b) C-band.

As shown in Fig. 9(a), when there is snow cover on the sea ice, the polarization ratio of the L-band radar for sea ice increases with the incident angle increasing, and decreases with the RMS height of the snow surface increasing. When the incident angle is less than 60°, the decrease can be neglected (less than 1 dB); that is, the L-band sea ice polarization ratio does not vary with the RMS height of snow surface. In Fig. 9(b), when the incident angle is smaller than 50°, the polarization ratio of the C-band radar scattering on the sea ice increases as the incident angle increases; and when the incident angle is larger than 50°, it decreases as the incident angle increases. When the incident angle is less than 60°, the sea ice polarization ratio increases with the RMS height of snow surface increasing. When the incident angle is greater than 60°, the sea ice polarization ratio decreases with the RMS heightening. Comparing with C-band radar, the effect of the snow surface RMS height on the L-band sea ice polarization ratio is negligible. It can be seen from Fig. 10 that the influence of the correlation length variation on the polarization ratio of the sea ice for C-band and L-band are negligible.

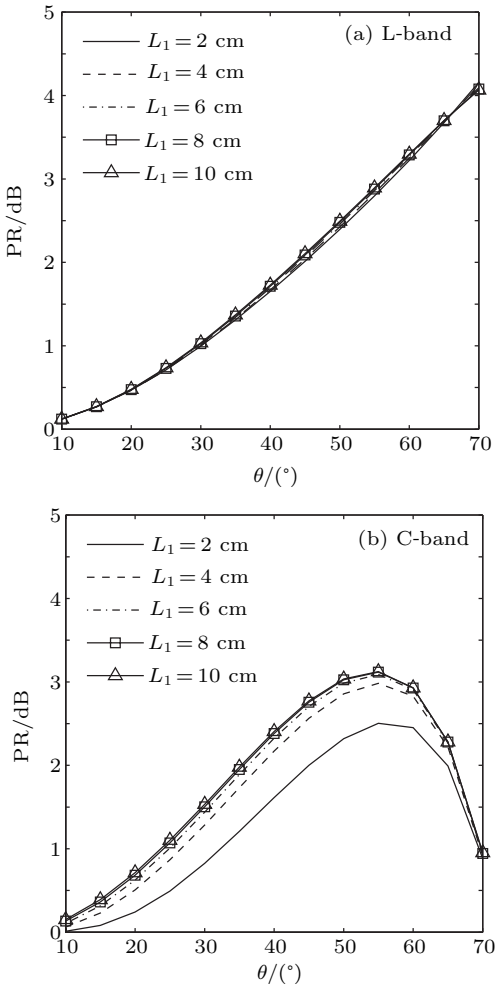


Fig. 10. Variations of snow-covered sea ice polarization ratio with correlation length of snow surface for (a) L-band and (b) C-band.

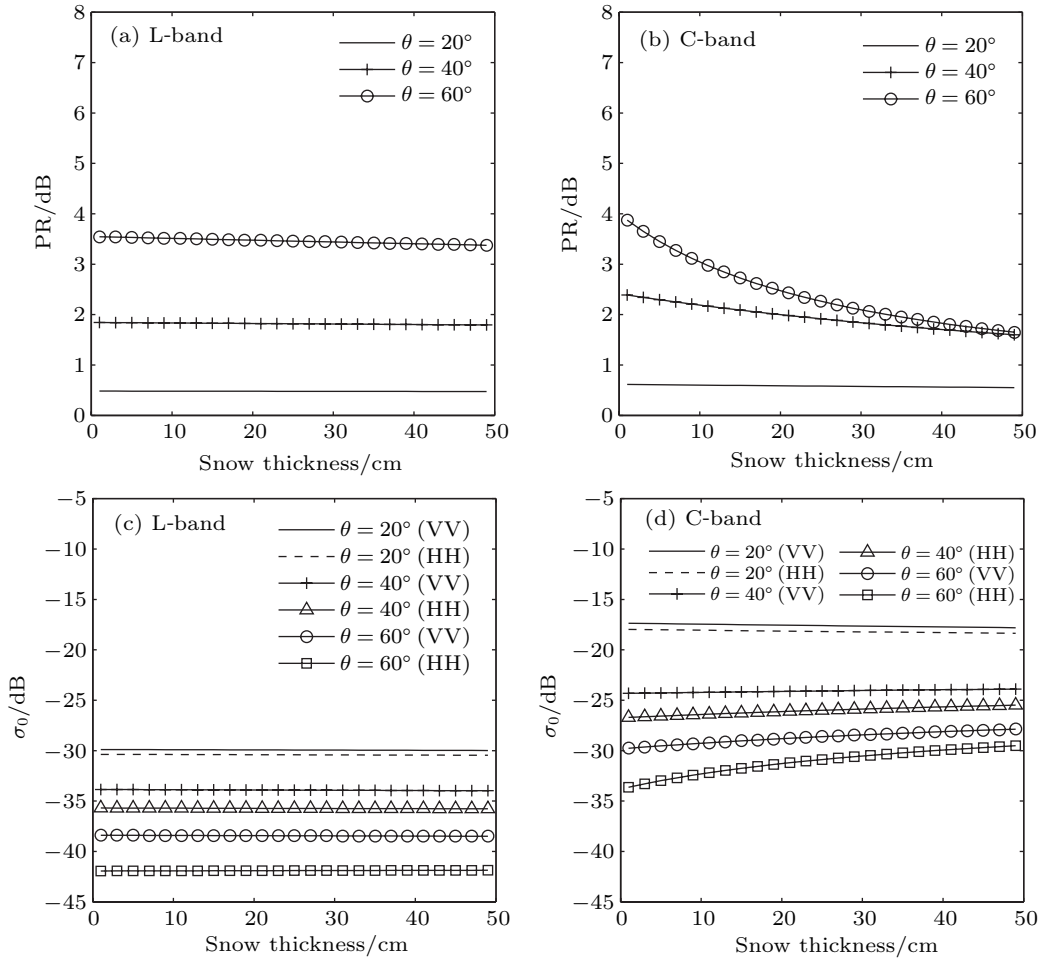


Fig. 11. Variations of snow-covered sea ice polarization ratio with snow thickness at three typical incident angles for (a) L-band and (b) C-band, and corresponding variations of backscattering coefficients for (c) L-band and (d) C-band.

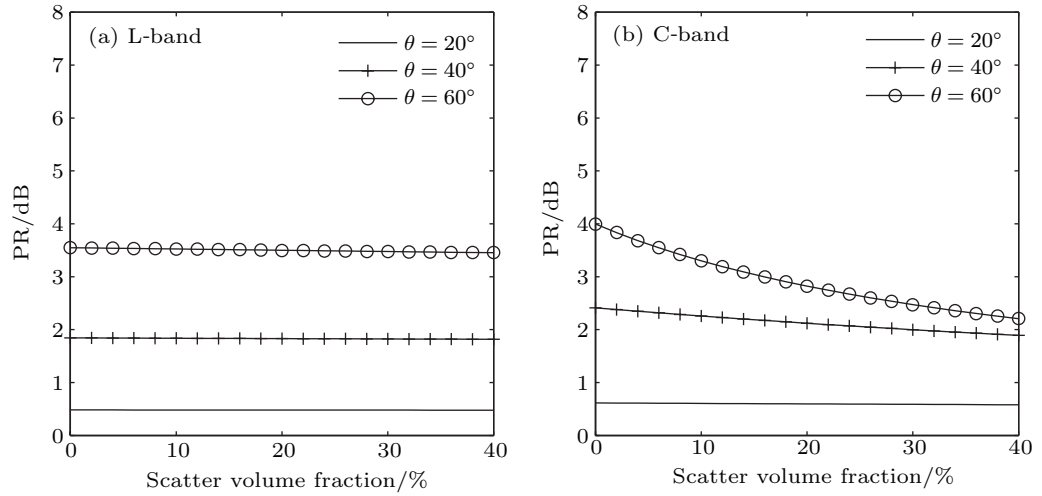


Fig. 12. Variations of snow-covered sea ice polarization ratio with scatterer volume fraction at three typical incident angles for: (a) L-band and (b) C-band.

The variations of sea ice polarization ratio with snow thickness at three typical incident angles are shown in Fig. 11. The L-band sea ice polarization ratio does not vary with snow thickness while the C-band sea ice polarization ratio decreases with snow thickness increasing. At small-to-medium incident angles, the influence of snow thickness on C-band sea ice polarization ratio is negligible due to the relevant mechanism for the dominant surface scattering in this angular region. For L-band, the backscattering coefficient of snow-covered sea ice shown in Fig. 11(c) does not change with snow thickness either. For C-band, in Fig. 11(d), with the increasing of snow thickness, the backscattering coefficient of sea ice remains constant at small-to-medium incident angle and increases at large incident angle. The backscattering coefficient of snow-

covered sea ice decreases with incident angle increasing. The reasons for these results have been described earlier.

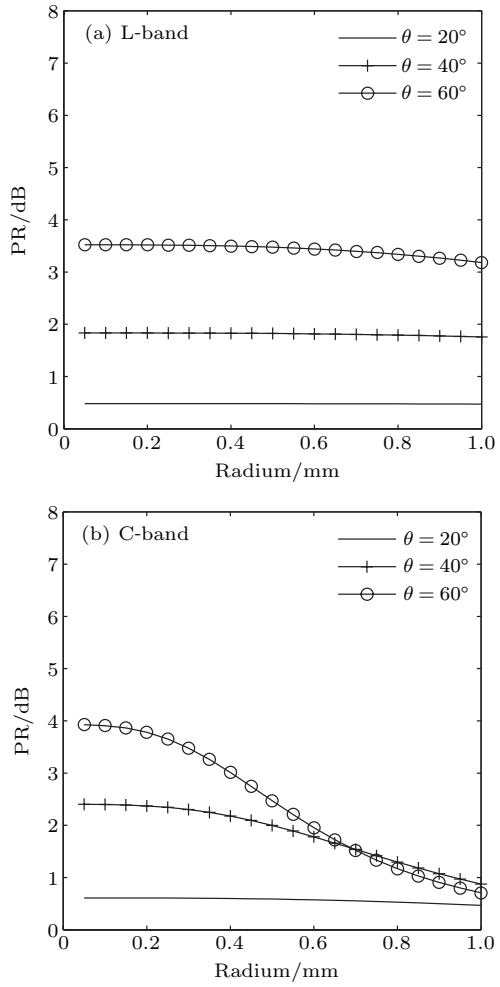


Fig. 13. Variations of snow-covered sea ice polarization ratio with scatterer radius at three typical incident angles for (a) L-band and (b) C-band.

As shown in Fig. 12(a), at three typical incident angles, the L-band sea ice polarization ratio does not change with scatterer volume fraction. At a small incident angle (20°) and medium incident angle (40°), the C-band sea ice polarization ratio hardly changes with the scatterer volume fraction; at a large incident angle (60°), the C-band sea ice polarization ratio decreases with scatterer volume fraction. The variation of the sea ice polarization ratio with scatterer radius is shown in Fig. 13. The L-band sea ice polarization ratios do not change with the scatterer radius in three cases, while the C-band sea ice polarization ratios do not change with the radius of scatterer at a small incident angle (20°) and decreases with the scatterer radius at a medium incident angle (40°) and large incident angle (60°).

3.4. Comparison between polarization ratios of seawater and sea ice

For the L-Band, according to this analysis, we find that the seawater polarization ratio only depends on incident angle, while the sea ice polarization ratio is mainly affected by incident angle and ice thickness. The influence of other factors on it is negligible. Figure 14(a) shows the variations of L-band polarization ratio with incident angle for sea water, bare sea ice with different thickness and snow-covered sea ice. It can be seen that there is obvious difference between the sea water polarization ratio and the sea ice polarization ratio in Fig. 14(b). The larger the incident angle and the ice thickness, the greater the difference between them will be. When the incident angle exceeds 40°, the polarization ratio can be used to distinguish between sea water and sea ice. When snow covers the sea ice, the difference between the polarization ratios of sea ice and sea water increases, making it easier to distinguish between sea water and sea ice.

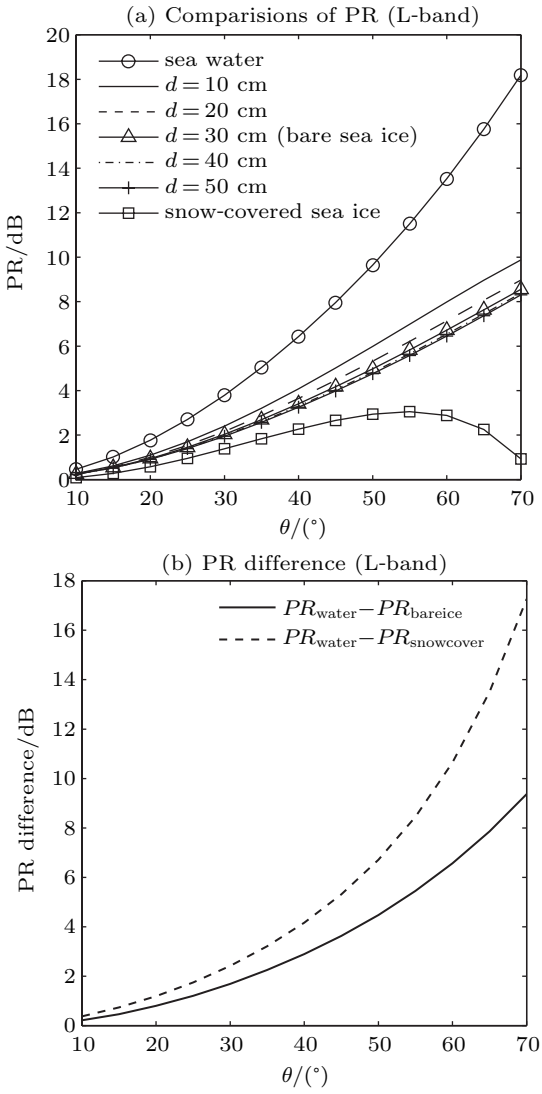


Fig. 14. For L-band, (a) variations of the polarization ratio with incident angle for seawater, bare and snow-covered sea ice and (b) their difference varying with incident angle.

For the C-band, the polarization ratio for radar scattering on bare sea ice is mainly related to the incident angle, RMS height and ice thickness, and decreases with the ice thickness. When the ice thickness reaches 10 cm, the sea ice polarization ratio no longer changes because the ice thickness is generally more than 10 cm in polar areas, and the effect of ice thickness

is negligible. Therefore, it is only necessary to compare the sea ice polarization ratios under different incident angles and RMS heights. As shown in Fig. 15, the solid line indicates the sea ice polarization ratio, and the dashed line refers to the seawater polarization ratio. Figure 15(b) shows the mean PR difference between sea water and sea ice for C-band. When the incident angle is less than 40°, the mean PR difference is quite small; when the incident angle exceeds 40°, the mean PR difference for C-band increases with the incident angle. Therefore, for C-band, sea ice and sea water can be discriminated by the polarization ratio at medium-to-large incident angles.

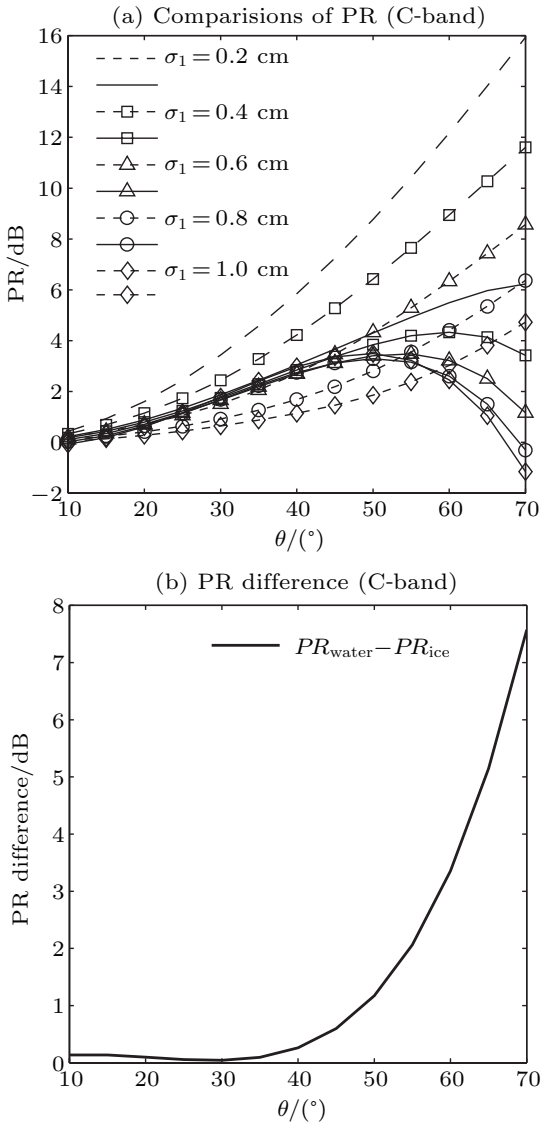


Fig. 15. For C-band: (a) Variations of polarization ratio for seawater, and sea ice with incident angle and (b) their difference varying with incident angle.

4. Conclusions and perspectives

The influence of polar sea ice on the climate has increasingly received attention. The wide-area monitoring of sea ice in the polar region has become the key to studying sea ice. Although the relevant research on sea ice monitoring by SAR has made some progress in recent years, there is still a technical bottleneck in distinguishing the automatic images of sea ice and seawater. Therefore, it is necessary to study the electromagnetic scattering mechanism for each of sea ice and sea water. Based on the electromagnetic scattering model derived from IEM and RT, the polarization ratios of seawater, bare sea ice and snow-covered sea ice are numerically simulated under different physical conditions. Their polarization ratio characteristics are analyzed.

Our numerical results indicate that the L-band seawater polarization ratio is only related to the incident angle and increases with incident angle increasing. The L-band sea ice polarization ratio is mainly affected by the incident angle and ice thickness, and decreases as ice thickness increases. After the ice thickness reaches a certain critical value, it no longer changes. This is mainly related to the L-band penetration depth for sea ice. Moreover, the sea ice penetration depth at L-band is larger than that of C-band. At C-band, the seawater polarization ratio is affected by incident angle and RMS height of sea surface, and increases with these two variables increasing; the bare sea ice polarization ratio is mainly related to incident angle, RMS height and ice thickness. When the incident angle exceeds 45°, the effect of RMS height on bare sea ice polarization ratio is negligible. When there is snow on the sea ice, the sea ice polarization ratio decreases, and the L-band sea ice polarization ratio is only related to the incident angle. By comparison, the C-band sea ice polarization ratio is affected by incident angle, RMS height of snow surface, snow thickness, volume fraction and radius of scatterers.

For the L-band radar, the difference between the polarization ratios of sea water and sea ice is obvious and increases with incident angle increasing. For the C-band radar, when the incident angle exceeds 40°, the difference between the polarization ratios of seawater and sea ice is also obvious and increases with incident angle increasing. Therefore, the sea ice and sea water can be distinguished using this property, which means that the recognition and classification algorithm for sea ice and open water does not rely on the remote sensing image itself. This provides theoretical support and technical means for further exploring the sea ice classification mechanism.

Appendix A: Shadowing function

The shadowing function proposed by Sancer[31] is a function of incident angle, θ, scattering angle, θ_s, and surface root mean square slope, σ_s, which can be written in the following form:

$$S(\theta,\theta_s) = [1 + f(\theta,\sigma_s) + f(\theta_s,\sigma_s)]^{-1}, \tag{A1}$$

$$f(\theta,\sigma_s) = \frac{1}{2}\left\{\sqrt{\frac{2}{\pi}}\frac{\sigma_s}{\cot\theta}\exp\left(-\frac{\cot^2\theta}{2\sigma_s^2}\right) - \mathrm{erfc}\left(\frac{\cot\theta}{\sqrt{2}\sigma_s}\right)\right\}, \tag{A2}$$

where erfc is the error-function complement related to the error function erf by

$$\mathrm{erfc}\,(x) = 1 - \mathrm{erf}\,(x) = \frac{2}{\sqrt{\pi}} \int_x^{\infty} \mathrm{e}^{-t^2}\,\mathrm{d}t. \tag{A3}$$

Appendix B: Correlation function

The following exponential correlation function is used in our work:

$$\rho = \exp(-|\,\xi\,|/L)\,, \tag{B1}$$

where ξ and L are the surface height and correlation length, respectively. The corresponding roughness spectrum is

$$W(K) = L^2[1+(KL)^2]^{-1.5}, \tag{B2}$$

and the Fourier transform of the n-th power of the correlation function is

$$\begin{aligned} W^{(n)}(K) &= \int_0^{\infty} \rho^n(\xi)\, J_0(K\xi)\, \xi\,\mathrm{d}\xi \\ &= \left(\frac{L}{n}\right)^2 \left[1+\left(\frac{KL}{n}\right)^2\right]^{-1.5}. \end{aligned} \tag{B3}$$

Appendix C: Expression for I^n_{pp}

I^n_{pp} has the following form:[26]

$$\begin{aligned} I^n_{\mathrm{pp}} &= (k_{sz}+k_z)^n f_{\mathrm{pp}} \exp\left(-\sigma^2 k_z k_{sz}\right) \\ &\quad + \frac{(k_{sz})^n F_{\mathrm{pp}}(-k_x,-k_y) + (k_z)^n F_{\mathrm{pp}}(-k_{sx},-k_{sy})}{2}, \end{aligned} \tag{C1}$$

$$\begin{aligned} f_{\mathrm{vv}} &= \frac{2R_{\mathrm{v}}}{\cos\theta+\cos\theta_{\mathrm{s}}}[\sin\theta\sin\theta_{\mathrm{s}} \\ &\quad - (1+\cos\theta\cos\theta_{\mathrm{s}})\cos(\phi_{\mathrm{s}}-\phi)], \end{aligned} \tag{C2}$$

$$\begin{aligned} f_{\mathrm{hh}} &= -\frac{2R_{\mathrm{h}}}{\cos\theta+\cos\theta_{\mathrm{s}}}[\sin\theta\sin\theta_{\mathrm{s}} \\ &\quad - (1+\cos\theta\cos\theta_{\mathrm{s}})\cos(\phi_{\mathrm{s}}-\phi)], \end{aligned} \tag{C3}$$

where R_{v} and R_{h} are Fresnel reflection coefficients, and

$$R_{\mathrm{v}} = \frac{\varepsilon_{\mathrm{r}}\cos\theta - \sqrt{\mu_{\mathrm{r}}\varepsilon_{\mathrm{r}} - \sin^2\theta}}{\varepsilon_{\mathrm{r}}\cos\theta + \sqrt{\mu_{\mathrm{r}}\varepsilon_{\mathrm{r}} - \sin^2\theta}}, \tag{C4}$$

$$R_{\mathrm{h}} = \frac{\mu_{\mathrm{r}}\cos\theta - \sqrt{\mu_{\mathrm{r}}\varepsilon_{\mathrm{r}} - \sin^2\theta}}{\mu_{\mathrm{r}}\cos\theta + \sqrt{\mu_{\mathrm{r}}\varepsilon_{\mathrm{r}} - \sin^2\theta}}. \tag{C5}$$

The relative permeability and permittivity of the rough surface are μ_{r} and ε_{r}, respectively,

$$\begin{aligned} &F_{\mathrm{vv}}(-k_x,-k_y) \\ &= \frac{\left(\mu_{\mathrm{r}}\varepsilon_{\mathrm{r}} - \sin^2\theta - \varepsilon_{\mathrm{r}}\cos^2\theta\right)(1+R_{\mathrm{v}})^2}{(\varepsilon_{\mathrm{r}}\cos\theta)^2\cos\theta_{\mathrm{s}}} \\ &\quad \times \sin\theta[\sin\theta_{\mathrm{s}} - \sin\theta\cos(\phi_{\mathrm{s}}-\phi)], \end{aligned} \tag{C6}$$

$$\begin{aligned} &F_{\mathrm{hh}}(-k_x,-k_y) \\ &= -\frac{\left(\mu_{\mathrm{r}}\varepsilon_{\mathrm{r}} - \sin^2\theta - \mu_{\mathrm{r}}\cos^2\theta\right)(1+R_{\mathrm{h}})^2}{(\mu_{\mathrm{r}}\cos\theta)^2\cos\theta_{\mathrm{s}}} \\ &\quad \times \sin\theta[\sin\theta_{\mathrm{s}} - \sin\theta\cos(\phi_{\mathrm{s}}-\phi)], \end{aligned} \tag{C7}$$

$$\begin{aligned} &F_{\mathrm{vvs}}(-k_{sx},-k_{sy}) \\ &= (1-R_{\mathrm{v}}^2)\left\{\left(\frac{1}{r_{\mathrm{cs}}}-1\right)\cos\theta_{\mathrm{s}}\cos(\phi_{\mathrm{s}}-\phi)\right. \\ &\quad + \frac{(1-r_{\mathrm{cs}})[\cos(\phi_{\mathrm{s}}-\phi) - \sin\theta\sin\theta_{\mathrm{s}}]}{\cos\theta} \\ &\quad \left. + \frac{(\varepsilon_{\mathrm{r}}-r_{\mathrm{cs}})\sin\theta_{\mathrm{s}}[\sin\theta - \sin\theta_{\mathrm{s}}\cos(\phi_{\mathrm{s}}-\phi)]}{sq}\right\}, \end{aligned} \tag{C8}$$

$$\begin{aligned} &F_{\mathrm{hhs}}(-k_{sx},-k_{sy}) \\ &= -(1-R_{\mathrm{h}}^2)\left\{\left(\frac{1}{r_{\mathrm{cs}}}-1\right)\cos\theta_{\mathrm{s}}\cos(\phi_{\mathrm{s}}-\phi)\right. \\ &+ \frac{(1-r_{\mathrm{cs}})[\cos(\phi_{\mathrm{s}}-\phi) - \sin\theta\sin\theta_{\mathrm{s}}]}{\cos\theta} \\ &\quad \left. + \frac{(\mu_{\mathrm{r}}-r_{\mathrm{cs}})\sin\theta_{\mathrm{s}}[\sin\theta - \sin\theta_{\mathrm{s}}\cos(\phi_{\mathrm{s}}-\phi)]}{sq}\right\}, \end{aligned} \tag{C9}$$

where $r_{\mathrm{cs}} = (\cos\theta_{\mathrm{s}}/\cos\theta)(sq/sq_{\mathrm{s}})$ and $sq = \sqrt{\mu_{\mathrm{r}}\varepsilon_{\mathrm{r}} - \sin^2\theta}$, and $sq_{\mathrm{s}} = \sqrt{\mu_{\mathrm{r}}\varepsilon_{\mathrm{r}} - \sin^2\theta_{\mathrm{s}}}$.

Appendix D: Rayleigh parameters

Suppose that the scatterer is a Rayleigh scatterer. Its radius is r_{s}, its relative dielectric constant is $\varepsilon_{\mathrm{s}} = \varepsilon_{\mathrm{sr}} - \mathrm{j}\varepsilon_{\mathrm{si}}$ and its volume fraction is f_{v}. The relative dielectric constant of the ambient medium is $\varepsilon_{\mathrm{b}} = \varepsilon_{\mathrm{br}} - j\varepsilon_{\mathrm{bi}}$. The absorption coefficient κ_{a}, and volume scattering coefficient are related by[27]

$$\kappa_{\mathrm{a}} = 2k_{\mathrm{bi}}(1-fv) + fvk_{\mathrm{br}}\frac{\varepsilon_{\mathrm{si}}}{\varepsilon_{\mathrm{br}}}\left|\frac{3\varepsilon_{\mathrm{b}}}{\varepsilon_{\mathrm{s}}+2\varepsilon_{\mathrm{b}}}\right|^2, \tag{D1}$$

where k_{br} and k_{bi} are the real and imaginary part of the host medium wave number $k\sqrt{\varepsilon}_{\mathrm{b}}$, and k is the wave number in free space.

$$\kappa_{\mathrm{s}} = \frac{8}{3}\pi N k_{\mathrm{br}}^4 r_{\mathrm{s}}^6 \left|\frac{\varepsilon_{\mathrm{s}}-\varepsilon_{\mathrm{b}}}{\varepsilon_{\mathrm{s}}+2\varepsilon_{\mathrm{b}}}\right|^2, \tag{D2}$$

where N is the number density related to the volume fraction fv by

$$N = \frac{3fv}{4\pi r_{\mathrm{s}}^3}. \tag{D3}$$

The extinction coefficient κ_{e}, the albedo a, and the optical depth τ of the Rayleigh layer are defined as follows:

$$\kappa_{\mathrm{e}} = \kappa_{\mathrm{a}} + \kappa_{\mathrm{s}}, \tag{D4}$$

$$a = \kappa_{\mathrm{s}}/\kappa_{\mathrm{e}}, \tag{D5}$$

$$\tau = \kappa_{\mathrm{e}} d, \tag{D6}$$

where d is the depth of layer.

References

[1] Zhang B, Perrie W, Vachon P W, Li X, Pichel W G, Guo J and He Y J 2012 *IEEE Trans. Geosci. Remote Sens.* **50** 4252

[2] Xie T, Perrie W, Fang H, Zhao L, Yu W J and He Y J 2017 *Chin. Phys. B* **26** 054102

[3] Lupidi A, Staglianò D, Martorella M and Berizzi F 2017 *Remote Sens.* **9** 230

[4] Fallahpour M B, Dehghani H, Jabbar Rashidi A and Sheikhi A 2018 *Int. J. Electron.* **105** 771

[5] Xie T, Perrie W, Fang H, Zhao L, Yu W J and He Y J 2017 *Sci. China Earth Sci.* **5** 1

[6] Fang H, Xie T, Perrie W, Zhao L, Yang J S and He Y J 2017 *Remote Sens.* **9** 1321

[7] Xie T, Zhao S Z, Perrie W, Fang H, Yu W J and He Y J 2016 *Chin. Phys. B* **25** 064101

[8] Xie T, Perrie W, Zhao S Z, Fang H, Yu W J and He Y J 2016 *Chin. Phys. B* **25** 074102

[9] Ochilov S & Clausi D A 2012 *IEEE Trans. Geosci. Remote Sens.* **50** 4397

[10] Zakhvatkina N Y, Alexandrov V Y, Johannessen O M, Sandven S & Frolov I Y 2013 *IEEE Trans. Geosci. Remote Sens.* **51** 2587

[11] Leigh S, Wang Z & Clausi D A 2014 *IEEE Trans. Geosci. Remote Sens.* **52** 5529

[12] Ressel R, Frost A & Lehner S 2015 *IEEE J. Sel. Top. Appl. Earth Observ. Remote Sens.* **8** 3672

[13] Singha S, Johansson M, Hughes N, Hvidegaard S M & Skourup H 2018 *IEEE Trans. Geosci. Remote Sens.* **56** 3715

[14] Bogdanov A V, Sandven S, Johannessen O M, Alexandrov V Y and Bobylev L P 2005 *IEEE Trans. Geosci. Remote Sens.* **43** 1648

[15] Vapnik V, Levin E and Cun Y L 1994 *Neural Comput.* **6** 851

[16] Liu H, Guo H and Zhang L 2015 *IEEE JSTARS* **8** 1601

[17] Ulaby F T, Moore R K and Fung A K 1982 *Microwave Remote Sensing*, Vol. 2 (Norwood, MA: Artech House) p. 962

[18] Tsang L, Kong J A and Shin R T 1985 *Theory of Microwave Remote Sensing* (New York: WileyInterscience)

[19] Fung A K 1994 *Microwave Scattering and Emission Models and Their Applications* (Norwood, MA: Artech House)

[20] Tsang L and Kong J A 2001 *Scattering of Electromagnetic Waves: Advanced Topics* (New York: Wiley)

[21] Broschat S L 1993 *IEEE Trans. Geosci. Remote Sens.* **31** 1112

[22] Voronovich A G 1994 *Waves Random Media* **4** 337

[23] Irisov V G 1997 *Waves Random Media* **7** 1

[24] Johnson J T 2002 *IEEE Trans. Geosci. Remote Sens.* **40** 500

[25] Fung A K, Li Z and Chen K S 1992 *IEEE Trans. Geosci. Remote Sens.* **30** 356

[26] Fung A K, Liu W Y, Chen K S and Tsay M K 2002 *J. Electromagnet. Wave* **16** 689

[27] Fung A K and Chen K S 2010 *Microwave Scattering and Emission Models for Users* (Norwood, MA: Artech House)

[28] Wakabayashi H, Matsuoka T, Nakamura K and Nishio F 2004 *IEEE Trans. Geosci. Remote Sens.* **42** 2412

[29] Liu M J, Dai Y S, Zhang J, Zhang X, Meng J M, Zhu X Q and Yin Y L 2016 *Acta Oceanol. Sin.* **35** 89

[30] Nakamura K, Wakabayashi H, Uto S, Naoki K, Nishio F and Uratsuka S 2006 *Ann. Glaciol.* **44** 261

[31] Syahali S & Ewe H T 2016 *Prog. Electromagn. Res. M* **48** 25

[32] Sancer M I 1969 *IEEE Trans. Anten. Propag.* **17** 577